Journal of Environmental Science International
29(1); 95~108; January 2020

pISSN: 1225-4517 eISSN: 2287-3503
https://doi.org/10.5322/JESI.2020.29.1.95

**ORIGINAL ARTICLE**

# Application of Nanoroll-Type Ag/g-$C_3N_4$ for Selective Conversion of Toxic Nitrobenzene to Industrially-Valuable Aminobenzene

Perumal Devaraji, Wan-Kuen Jo*

*Department of Environmental Engineering, Kyungpook National University, Daegu 41566, Korea*

## Abstract

Silver nanoparticles were loaded onto g-$C_3N_4$ (CN) with a nanoroll-type morphology (Ag/CN) synthesized using a co-polymerization method for highly selective conversion of toxic nitrobenzene to industrially-valuable aminobenzene. Scanning electron microscopy and high-resolution transmission electron microscopy (HRTEM) images of Ag/CN revealed the generation of the nanoroll-type morphology of CN. Additionally, HRTEM analysis provided direct evidence of the generation of a Schottky barrier between Ag and CN in the Ag/CN nanohybrid. Photoluminescence analysis and photocurrent measurements suggested that the introduction of Ag into CN could minimize charge recombination rates, enhancing the mobility of electrons and holes to the surface of the photocatalyst. Compared to pristine CN, Ag/CN displayed much higher ability in the photocatalytic reduction of nitrobenzene to aminobenzene, underscoring the importance of Ag deposition on CN. The enhanced photocatalytic performance and photocurrent generation were primarily ascribed to the Schottky junction formed at the Ag/CN interface, greater visible-light absorption efficiency, and improved charge separation associated with the nanoroll morphology of CN. Ag would act as an electron sink/trapping center, enhancing the charge separation, and also serve as a good co-catalyst. Overall, the synergistic effects of these features of Ag/CN improved the photocatalytic conversion of nitrobenzene to aminobenzene.

**Key words** : Toxic nitrobenzene, Industrially-valuable aminobenzene, Schottky barrier, Nanoroll-type morphology

## 1. Introduction

Nitrobenzene (NBZ) is a highly toxic organic compound towards human health and ecological system (European Chemical Agency, 2012). Aminobenzene (ABZ) and other aromatic amine compounds are very valuable chemical species that are widely used as intermediates for many drugs, fragrances, and dyes in chemical industries. Aromatic amine compounds can be produced through catalytic or photocatalytic reduction of nitroaromatic compounds (Tada et al., 2005; Grirrane et al., 2008; Zhu et al., 2010; Kimura et al., 2012; Chen et al., 2013; Ke et al., 2013; Tanaka et al., 2013; Toyao et al., 2013; Xiao et al., 2016; Chaiseeda et al., 2017). Zhu found that Surface Plasmon Resonance (SPR) phenomena of precious metals induce the generation of hot electrons upon light illumination, which can interact effectively with reactant molecules to enhance NBZ reduction over Au/$TiO_2$ (Zhu et al., 2010). Au particles on $TiO_2$ or $CeO_2$ can catalytically reduce NBZ to ABZ at 120 °C under a $H_2$ (9 bar) atmosphere (Grirrane et al.,

**Received** 3 December, 2019; **Revised** 15 January, 2020;
**Accepted** 21 January, 2020
***Corresponding author**: Department of Environmental Engineering, Kyungpook National University, Daegu 41566, Korea
Phone: +82-53-950-6584
E-Mail: wkjo@knu.ac.kr

2008). Chaiseeda et al.(2017) also reported improved photocatalytic reduction of NBZ under visible-light irradiation using Au supported on $Al_2O_3$ in the presence of a hole scavenger. Tanaka et al.(2013) reported that Ag nanoparticles could be used as a co-catalyst in a $Au/TiO_2$ photocatalytic system to enhance the reduction of NBZ to ABZ under visible-light irradiation, but led to acetone as a side product. Incorporating Ag to produce $Au/TiO_2$-Ag led to the enhancement of the stoichiometric reaction with few side products. Tada et al.(2005) reported that NBZ was adsorbed selectively on the surface of Ag nanoparticles rather than anatase-type $TiO_2$ in $Ag/TiO_2$ and showed the photocatalytic conversion of NBZ to ABZ under UV-light illumination. $Ag/TiO_2$ showed more activity in NBZ reduction than virgin $TiO_2$; thus, Ag nanoclusters act as a co-catalyst and enhance the selectivity for the target product (ABZ) (Tada et al., 2005). Several other catalysts for the reduction of NBZ include $Au/CeO_2$ (Ke et al., 2013), Au-Cu alloy (Xiao et al., 2016), Pt/Ti-metal-organic-framework-$NH_2$ (Toyao et al., 2013), $Au/TiO_2$ (Kimura et al., 2012), and a CdS/graphene hybrid nanocomposite (Chen et al., 2013). However, highly selective conversion of NBZ to ABZ without re-oxidation is a challenging task.

g-$C_3N_4$ (CN) is a well-known visible-light-active two-dimensional (2D) semiconductor material with a low band gap (2.7 eV). The $\pi$-conjugated double bonds in CN can facilitate fast transfer of charge carriers, which minimizes their recombination. An et al.(2016) carried out the photocatalytic conversion of nitrophenol to aminophenol using a Ag-loaded CN/chitosan composite in the presence of $NaBH_4$. Yang et al.(2017) prepared an MIL-125/Ag/CN nanocomposite photocatalyst for the reduction of various aromatic nitro compounds and reported 74% conversion of NBZ to ABZ under 4 h of visible-light illumination. CdS/CN with a 10 wt% CdS loading was able to catalyze the reduction of 49.2% of NBZ to ABZ with a 26% yield because of the synergic interaction between CdS and CN resulting in high charge transfer (Dai et al., 2014). Electronic integration of Ag, which has an SPR effect upon absorbing light at 500 nm and acts as a good co-catalyst for reduction reactions, into CN is an attractive approach for improving its absorption of visible light. The Schottky barrier between the metal and CN improves charge movement, and the transferred electrons are stored in the metal and utilized efficiently for the reduction reaction (Verma et al., 2017). A Ag@CN photocatalytic material was also used efficiently for the degradation of aqueous pollutants (Khan et al., 2018). Although many methods for the synthesis of high-conduction materials have been developed, establishment of methods for highly conductive semiconductors is yet a challenging research topic.

Tuning of a nanostructure to different morphologies can lead to enhanced photocatalytic activity (Zhang et al., 2012; Bai et al., 2013; Shiraishi et al., 2014; Tahir et al., 2014; Ho et al., 2015; Jin et al., 2015; Guo et al., 2016; Han et al., 2016; Devaraji and Gopinath, 2018). Many research groups have constructed 2D sheets of CN for photocatalytic applications. Shiraishi et al. synthesized sheet-like structured CN through calcination of cyanamide and reported the selective generation of $H_2O_2$ under visible-light irradiation (Shiraishi et al., 2014). Han et al. synthesized 2D single-atom CN nanosheets via calcination of freeze-dried dicyandiamide (DCDA) to produce $H_2$ from water (Han et al., 2016). We have synthesized 2D CN nanosheets through the co-polymerization of urea, and a Pt-CN-($Au/TiO_2$) nanocomposite gave high $H_2$ production (Devaraji and Gopinath, 2018).

Transformation of the 2D morphology to nanotubes (Guo et al., 2016), nanorolls (Ho et al., 2015), or nanorods may also induce high charge carrier mobility and increase charge separation, in turn improving the photocatalytic performance (Bai et al., 2013). Morphology control is very difficult, and obtaining a

specific structure requires additional or special treatment. Bai et al. attempted to prepare nanorod-type CN via ultrasonication followed by a subsequent reflux treatment for 48 h; during the reflux treatment, the surface defects could be eliminated and the CN nanoplates were transformed to nanorods (Bai et al., 2013). Jin et al. (2015) synthesized CN nanotubes via a condensation treatment of melamine; melamine was first treated hydrothermally at 200℃ for 24 h and then the obtained white powder was calcined to promote the formation of CN nanotubes. Tahir et al. fabricated CN nanofibers in two steps; melamine was treated with ethanol and $HNO_3$ to obtain white powder and then annealed at 450℃ for 2 h using a chemical vapor deposition process (Tajir et al., 2014). However, nanoroll-shaped photocatalysts have rarely been investigated, even though they can show higher photocatalytic activities than those of photocatalysts with other morphologies (Guo et al., 2017). Accordingly, we synthesized new nanoroll-type CN deposited with Ag nanoclusters using a co-polymerization and photodeposition process. The performance of the fabricated photocatalysts was assessed in terms of the photocatalytic conversion of toxic NBZ to industrially-valuable ABZ under visible-light illumination.

## 2. Experimental

### 2.1. Synthesis of polymeric CN

Melamine, silver nitrate ($AgNO_3 \cdot 3H_2O$), NBZ ($C_6H_5NO_2$), and ABZ ($C_6H_7N$) were purchased from Sigma-Aldrich. Briefly, 5 g of melamine was ground well with a mortar and pestle for 10 min and then transferred to a ceramic boat, which was heated to 550 °C in a $N_2$ atmosphere with a ramping rate of 2℃ $min^{-1}$. After the temperature reached 550℃, it was maintained for 5 h and then the sample was cooled. The obtained yellow powder was ground and named polymeric graphitic Carbon Nitride (CN).

### 2.2. Preparation of Ag–deposited CN

Photodeposition was used to deposit Ag nanoparticles onto the synthesized polymeric CN. In a 100-mL quartz round bottom flask, the required amounts of a silver nitrate solution and CN were mixed with 50 mL of $CH_3OH$. The above mixture was bubbled with $N_2$ for 1 h to remove any dissolved $O_2$ and to generate an inert atmosphere. Photoirradiation was conducted with a 400-W mercury UV lamp for 1 h. After photodeposition, the obtained powder sample was washed seven times with water and then dried at 80℃ for 15 h. Different amounts of Ag (varying from 0.1 to 1 wt%) were deposited on CN and the products were named $_x$Ag/CN; the subscript “x” denotes the wt% of Ag deposited on CN.

### 2.3. Characterization of synthesized photocatalysts

Structural properties of the as-synthesized materials were examined by various characterization methods, which includes Powder X-ray diffraction (PXRD), and the XRD data for all of the powder catalysts were recorded using a Rigaku (D/Max-2500) vertical type wide angle goniometer. The X-ray diffractometer used Cu K$\alpha$ (0.154 nm) at 3 $min^{-1}$ and 8 kW. BET -BELSORP Mini II surface area analyser was used to measure the surface area ($S_{BET}$) and porosities of the materials. The measurements were performed after degassing of the samples at 300℃. The Field Emission Scanning Electron Microscopy (FE-SEM), Energy -Dispersive X-ray (EDX) spectroscopy, high-resolution transmission electron microscopy (HRTEM), UV-visible absorption spectroscopy, Fourier transform infrared (FTIR), X-ray Photoelectron Spectroscopy (XPS), photoluminescence (PL) spectroscopy and photocurrent measurements were also conducted. The FE-SEM system (Hitachi SU8220) was equipped with an EDX attachment (Horiba X-MaxN with a silicon DRIFT X-ray detector) and used to examine the surface morphologies and chemical compositions of the prepared catalysts. Prior to SEM analysis, samples

were coated with indium by ion sputtering (Hitachi, E-1030) for 60 s. HRTEM was performed on the catalysts using an FEI Titan G2ChemiSTEM Cs Probe microscope. Diffuse reflectance UV-visible spectra were recorded using a Shimadzu UV-2600 spectrophotometer with $BaSO_4$ as a standard reference material. Raman analysis was carried out using a Renishaw (inVia reflex) spectrometer combined with a microscope in reflectance mode with a 632-nm excitation laser source and spectral resolution of 0.5 $cm^{-1}$.

XPS was performed using an ULVAC-PHI Quantera SXMTM scanning XPS microscope with an Al K$\alpha$ radiation source or a Kratos Axis HSi photoelectron spectrometer equipped with a charge neutralizer and a monochromatic Al K$\alpha$ (1486.6 eV) radiation source. PL measurements were performed using a Shimadzu RF-6000 with a tunable excitation wavelength. All PL measurements were performed with 350 nm excitation pulses. The transient photocurrent measurements were performed on an IVIUM Technologies electrochemical workstation in a three-electrode cell. Indium Tin Oxide (ITO) coated with a catalyst served as the working electrode. FTIR was performed on a PerkinElmer Frontier spectrophotometer between 400 and 4000 $cm^{-1}$ for samples diluted in KBR.

### 2.4. Photocatalytic activity tests

The photocatalytic reaction of NBZ over the synthesized photocatalysts was performed using a quartz reactor. Each photocatalyst (5 mg) was added to a nitrobenzene-methanol mixture (32 mL of 5 ppm nitrobenzene and 8 mL of methanol) to provide a reaction solution. One sun irradiation was provided by a solar simulator/300 W xenon lamp unit. Before illumination, the suspension was purged with ultrapure $N_2$ gas for 30 min. During illumination, liquid samples were analyzed periodically using a Shimadzu UV-2600 spectrophotometer.

## 3. Results and Discussions

### 3.1. X-ray diffraction (PXRD)

The structural properties of the synthesized materials were investigated using PXRD studies. Fig. 1 displays the PXRD patterns of CN, $_{0.1}$Ag/CN, $_{0.3}$Ag/CN, and $_{0.5}$Ag/CN. The PXRD patterns of CN and all $_x$Ag/CN samples showed two characteristic diffraction peaks at $2\theta$ = 13.04° and 27.2°, which correspond to the (100) and (002) planes of CN, respectively. The strong diffraction peak at $2\theta$ = 27.2° was attributed to the characteristic diffraction for a stack of aromatic groups, which was similar to that of graphite. A high-intensity XRD peak at 27.2° is characteristic for stacking of aromatic systems, while a peak at 13.04° corresponds to a packing structure (Bharad et al., 2015).

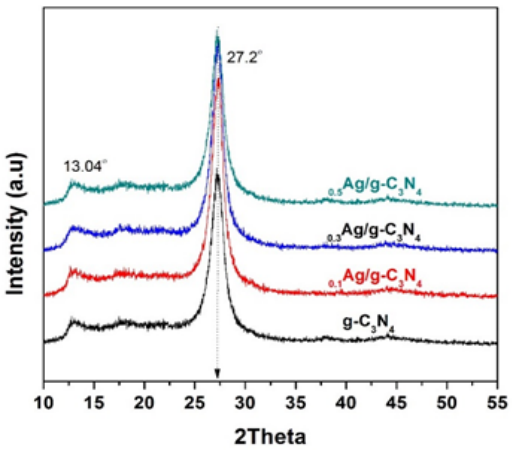


**Fig. 1.** PXRD pattern of CN, $_{0.1}$Ag/CN, $_{0.3}$Ag/CN, and $_{0.5}$Ag/CN.

### 3.2. Scanning Electron Microscopy (SEM) and High-Resolution Transmission Electron Microscopy (HRTEM) studies

The morphologies, textural properties, and Schottky junctions of the synthesized materials were investigated using SEM and HRTEM analyses. Fig. 2 shows the SEM and HRTEM images of CN and $_{0.5}$Ag/CN. The SEM images of CN (Fig. 2(a)) show a

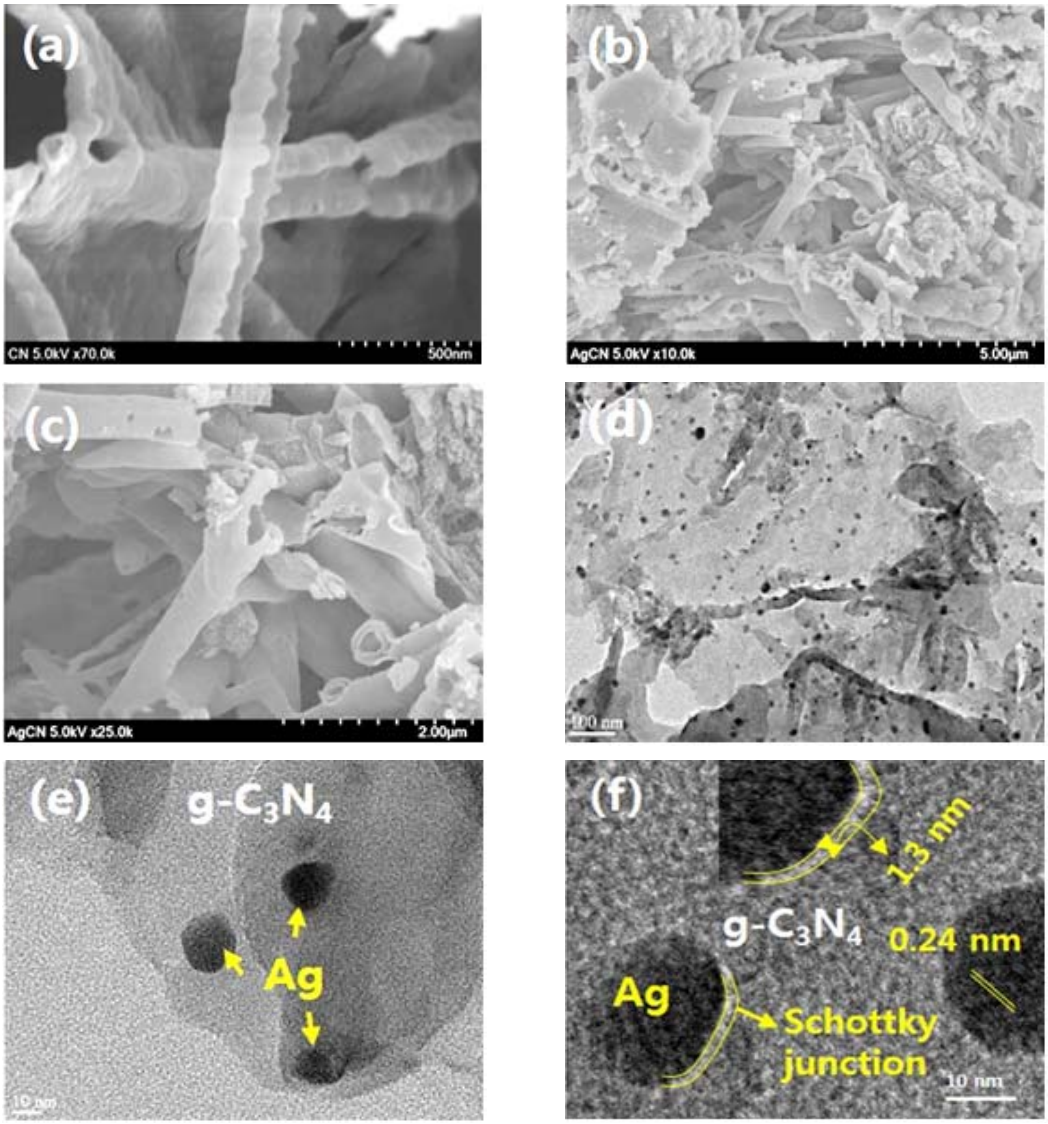


**Fig. 2.** SEM images of (a) CN, (b-c) $_{0.5}$Ag/CN, and (d-f) HRTEM images of $_{0.5}$Ag/CN.

predominant nanoroll shape and a half round-pipe -shape morphology. The nanoroll morphology was clearly visible in the SEM (Figs. 2(b) and (c)) and HRTEM (Fig. 2(d)) images of $_{0.5}$Ag/CN, indicating that Ag introduction did not change the morphology of CN. Along with the nanoroll morphology, sheet morphology was observed in CN (Fig. 3) and $_{0.5}$Ag/CN (Fig. 2(d)). Spherical Ag nanoparticles were highly dispersed on the surfaces of CN sheets and tubes (Figs. 2(d) and 2(e)). The nanoroll and 2D sheet morphologies of CN facilitate fast charge carrier transfer, while the $\pi$-conjugated double bonds in CN enhance charge separation (Bharad et al., 2015). Furthermore, the high transfer ability of the material indicated the existence of pores in the synthesized catalysts. The presence of highly dispersed Ag

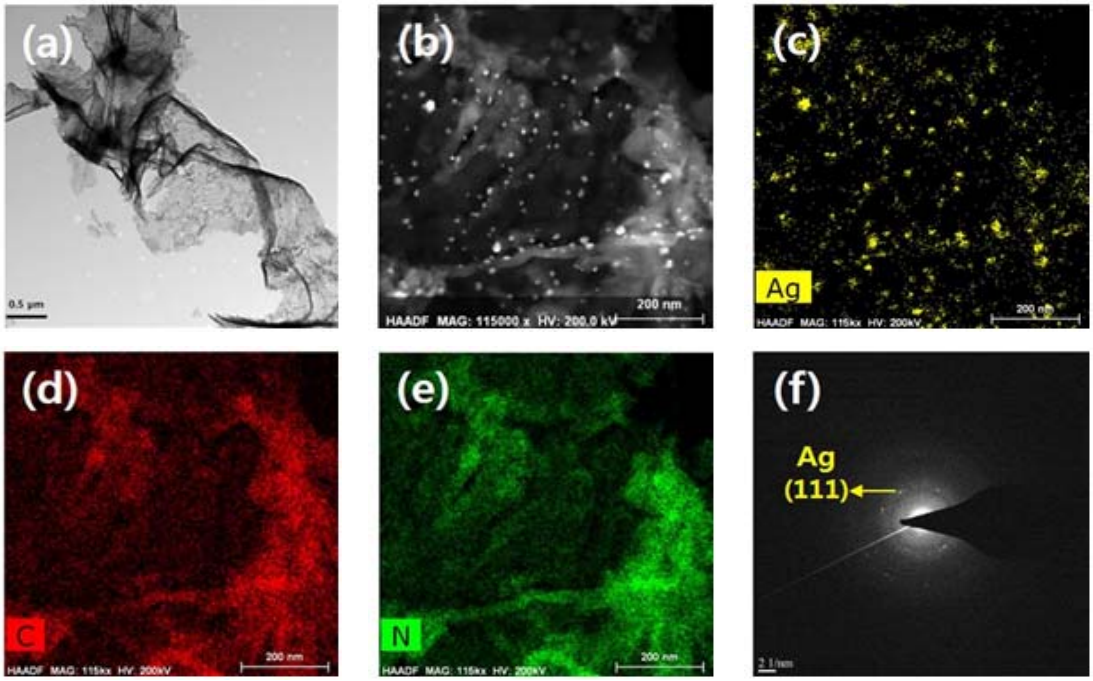


**Fig. 3.** HRTEM images of (a) g-$C_3N_4$, (b) $_{0.5}$Ag/g-$C_3N_4$, (c-e) and f the respective elemental mapping images and SAED pattern of $_{0.5}$Ag/g-$C_3N_4$ respectively. Color coding of each element was labeled on the respective elemental mapping images as Ag-yellow, C-red and N-green.

nanoparticles in $_{0.5}$Ag/CN highlighted the importance of the photodeposition reduction method. More importantly, Fig. 2(f) shows direct evidence of a Schottky junction (or Schottky barrier) at the Ag-CN interface in the $_{0.5}$Ag/CN material. The observed width of the Schottky barrier was 1.3 nm (Fig. 2(f) inset). The Ag nanoparticles displayed a d-spacing of 0.24 nm associated with the (111) plane of Ag (Patra and Gopinath, 2017). For more detailed analysis, elemental mapping (Figs. 3(b–e)) and selected area diffraction (SAED, Fig. 3(f)) were performed for $_{0.5}$Ag/CN; the observed SAED spots confirmed that Ag nanoparticles existed in the (111) plane. This observation was consistent with the results of PXRD analysis (Fig. 1). Direct contact between the (111) plane of Ag nanoparticles and the CN surface is essential for the separation of photogenerated charge carriers from the Schottky junction to the surface of the photocatalyst, where the photocatalytic reaction occurs (Devaji et al., 2014; Patra and Gopinath, 2017). Ag nanoparticles would act as electron-trapping centers. Therefore, the composite of Ag and CN could synergistically enhance the charge separation. In fact, this observation is in good agreement with photoluminescence (PL) results; Ag/CN displayed lower PL emission intensity compared to that of pure CN, indicating that the charge recombination was reduced after Ag deposition. Moreover, the observed sizes of the Ag nanoparticles were in the 7-23 nm range.

### 3.3. Surface area analysis

$N_2$ adsorption-desorption analysis was carried out to investigate the textural properties and porous natures of CN and the $_x$Ag/CN catalysts. Figs. 4(a–d) show the $N_2$ adsorption-desorption isotherms of the CN, $_{0.1}$Ag/CN, $_{0.3}$Ag/CN, and $_{0.5}$Ag/CN materials,

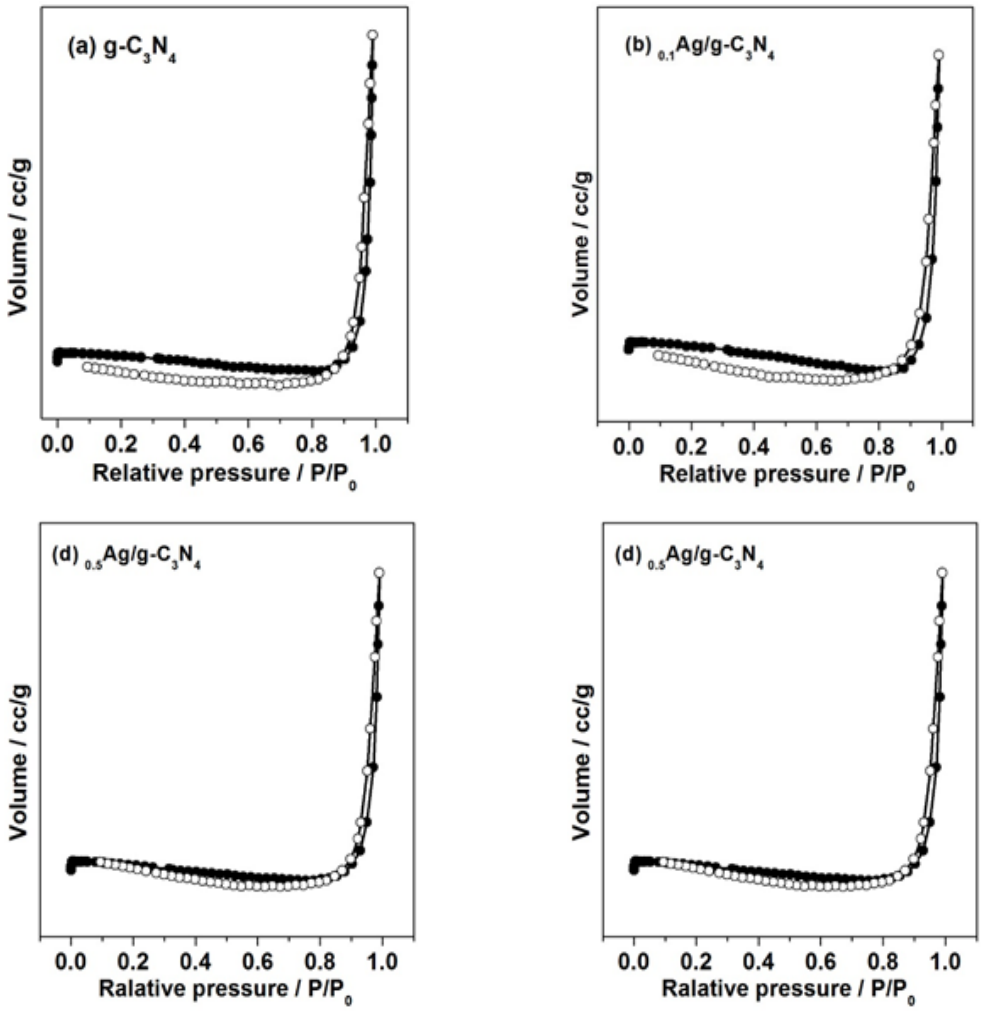


**Fig. 4.** $N_2$ adsorption-desorption isotherm studies of (a) CN, (b) $_{0.1}$Ag/CN, (c) $_{0.3}$Ag/CN, and (d) $_{0.5}$Ag/CN.

respectively. All of the samples gave a type IV adsorption-desorption isotherm with an H3 hysteresis loop. This result indicated that all synthesized materials were mesoporous. The obtained Brunauer -Emmett-Teller (BET) surface areas and pore volumes are given in Table 1. The surface areas of both CN and $_{0.1}$Ag/CN were approximately 6.1 $m^2$/g. There was no significant difference in the surface areas of these two materials, likely owing to a low Ag loading (0.1 wt%). The surface area of $_{0.3}$Ag/CN was 6.3 $m^2$/g, while that of $_{0.5}$Ag/CN was 7.6 $m^2$/g. The meso- and macroporosity was confirmed using the Barrett -Joyner-Halenda method. The total pore volume decreased significantly from 0.09 for CN to ~0.07 for $_x$Ag/CN, indicating that Ag nanoclusters were well dispersed and some of the Ag nanoparticles were located in the pores of CN.

### 3.4. UV–visible absorption spectroscopy

UV-visible absorption spectra were recorded to assess the optical properties of CN and the effect of Ag

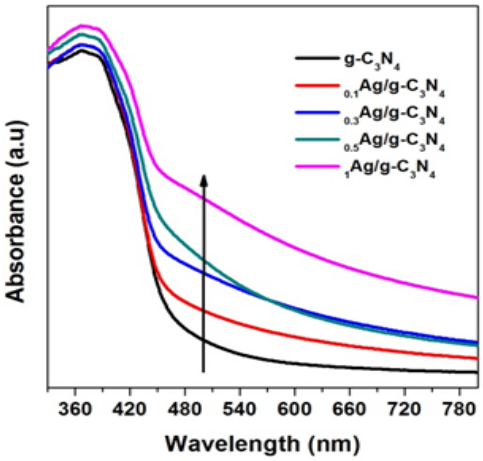


**Fig. 5.** UV-Vis absorption spectra of CN, $_{0.1}$Ag/CN, $_{0.3}$Ag/CN, $_{0.5}$Ag/CN, and $_{1}$Ag/CN.

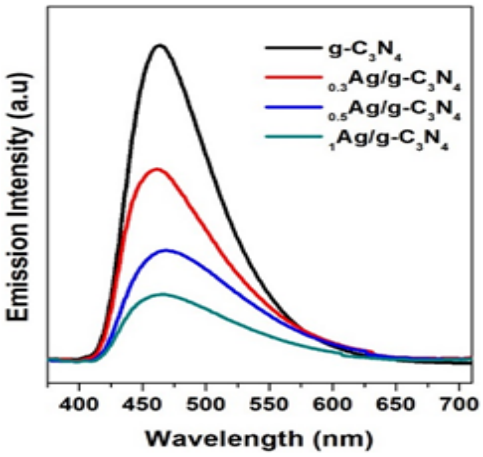


**Fig. 6.** Photoluminescence spectra of CN, $_{0.3}$Ag/CN, $_{0.5}$Ag/CN, and $_{1}$Ag/CN.

**Table 1.** Physicochemical properties of CN, $_{0.1}$Ag/CN, $_{0.3}$Ag/CN, and $_{0.5}$Ag/CN materials

| Sample | $S_{BET}$ ($m^2$/g) | Total pore volume ($cm^3$/g) |
|---|---|---|
| CN | 6.1 | 0.09 |
| 0.1Ag/ CN | 6.1 | 0.06 |
| 0.3Ag/ CN | 6.3 | 0.06 |
| 0.5Ag/ CN | 7.6 | 0.07 |

deposition. Fig. 5 shows the absorption spectra of CN, $_{0.1}$Ag/CN, $_{0.3}$Ag/CN, $_{0.5}$Ag/CN, and $_{1}$Ag/CN. Pristine CN showed absorption in the visible light region, corresponding to a band gap energy of 2.7 eV (Ge et al., 2011). Introduction of Ag into CN led to enhanced optical properties in all Ag/CN materials. Upon increasing the Ag loading from 0.1 to 1 wt%, improved visible light absorption was observed. The Ag-loaded CN samples showed an absorption maximum at ~500 nm (Li et al., 2017). The color of the materials changed (not shown) from yellow to dark gray when different amounts of Ag were deposited on CN, indicating changes in the optical properties of the photocatalysts.

### 3.5. Photoluminescence studies

Fig. 6 shows the PL emission properties of CN and all Ag-deposited CN photocatalysts. A strong peak at 463 nm was observed for CN. The deposition of Ag onto CN led to decreased intensities for the emission features. CN showed stronger emission features compared to those of reference photocatalysts, indicating fast recombination of photoinduced charge carriers. The Ag-deposited CN samples showed decreased PL emission intensities, mainly owing to effective charge transfer at the Schottky barrier. It is noteworthy that the Schottky junction can enhance the charge mobility at the metal-semiconductor interface (Patra et al., 2017). Moreover, the nanoroll-type CN and the Schottky barrier could synergistically enhance the mobility of the generated electrons and holes, which can be further utilized effectively for surface reactions. This process would increase the separation of generated charge carriers. Furthermore, the decreased PL intensity of Ag/CN indicated that Ag

nanoparticles acted as electron sinks that can trap the excited electrons effectively and minimize charge recombination (Sathu et al., 2016; Devaraji and Jo, 2018). These results are consistent with those of UV-visible absorption studies (Fig. 4).

### 3.6. Fourier transform infrared (FTIR) studies

The FTIR spectra of the CN, $_{0.1}$Ag/CN, $_{0.3}$Ag/CN, and $_{0.5}$Ag/CN materials are displayed in Fig. 7. Pristine CN and the $_x$Ag/CN samples gave a broad band at around 3000 $cm^{-1}$, which was indicative of N-H stretching vibration modes. The peaks at 1637 and 1243 $cm^{-1}$ corresponded to the typical C=N and C-N stretching vibration modes, respectively, and were similar to those reported in the literature (Kumar et al., 2013). Additionally, the characteristic vibration mode of the s-triazine units was observed at 804 $cm^{-1}$. A peak at 1384 $cm^{-1}$ could be attributed to the H-O-H bending band of surface-adsorbed $H_2O$ molecules (Devaraji and Gopinath, 2018).

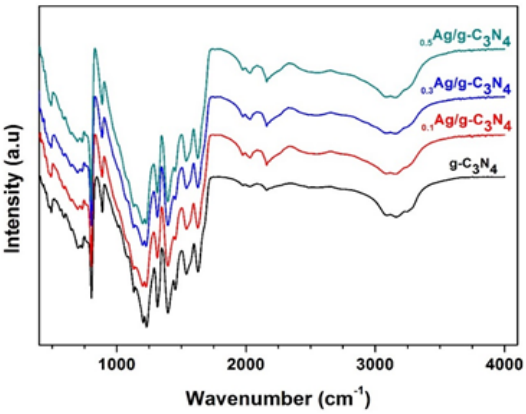


**Fig. 7.** FTIR spectra of CN, $_{0.1}$Ag/CN, $_{0.3}$Ag/CN, and $_{0.5}$Ag/CN.

### 3.7. X-ray Photoelectron Spectroscopy (XPS)

Fig. 8 shows the XPS core-level spectra of the CN and $_{0.5}$Ag/CN materials. In the C1s core-level spectra, the peaks observed at 284.1 and 287.7 eV for both CN and $_{0.5}$Ag/CN were ascribed to typical $sp^3$ and $sp^2$ carbons and carbons in $(N)_2$-C=N, respectively (Fig. 8(a)). As shown in Fig. 8(b), the N1s peak was found at ~398.2 eV and another peak appeared at ~400.5 eV, which was attributed to the tertiary nitrogen group, N-($C_3$) (Gholap et al., 2005). Introduction of Ag nanoparticles led to a decrease in the peak intensity in the N1s spectrum for $_{0.5}$Ag/CN, likely owing to interactions between nitrogen and the Ag nanoparticles. Additionally, the peaks that appeared at 366.9 (Ag $3d_{5/2}$) and 372.9 eV ($3d_{3/2}$) (Fig. 8(c)) were ascribed to the electronic interaction between metallic Ag nanoparticles and CN in $_{0.5}$Ag/CN (Li et al., 2017). The low-intensity PL emission features for $_{0.5}$Ag/CN strongly indicated a low charge recombination rate (Devaraji et al., 2017; Li et al., 2017).

### 3.8. Photocatalytic activity

The photocatalytic reduction of NBZ to ABZ was

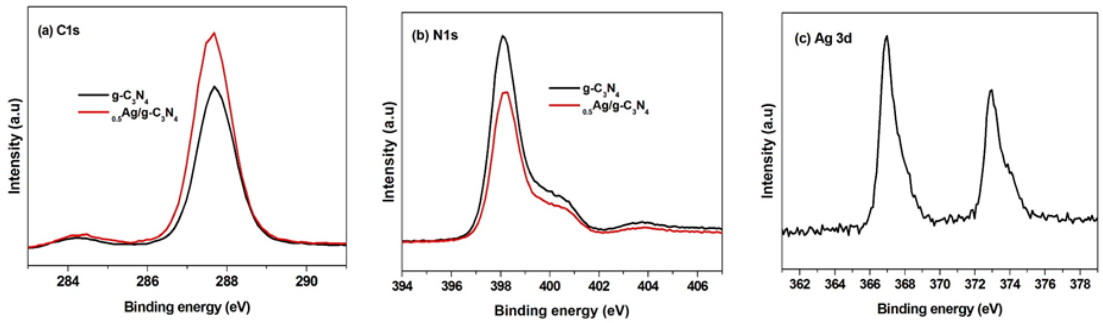


**Fig. 8.** XPS core level spectra of (a) C1s and (b) N1s of CN and $_{0.5}$Ag/CN and (c) Ag 3d core level of $_{0.5}$Ag/CN.

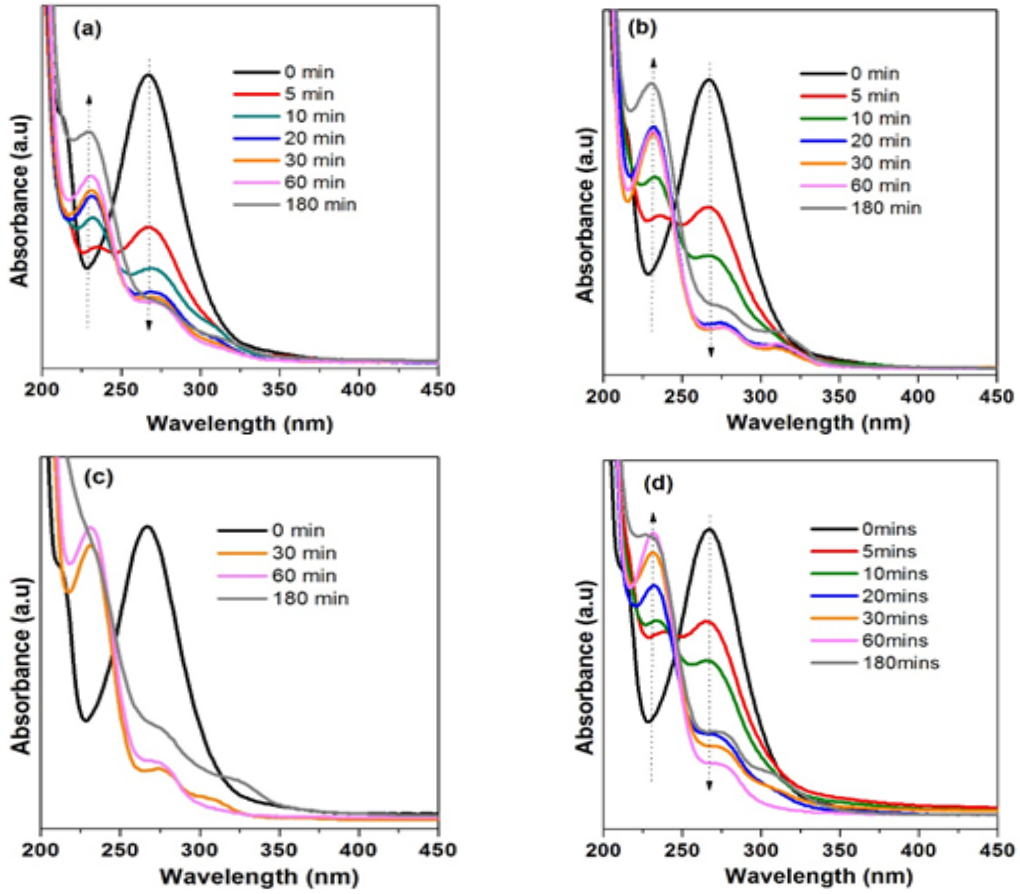


**Fig. 9.** UV-Visible absorption spectrum of photocatalytic NBZ to ABZ conversion with (a) $_{0.3}$Ag/CN, (b) $_{0.5}$Ag/CN, (c) $_{1}$Ag/CN, and (d) $_{2}$Ag/CN.

performed under a simulated solar light source (one sun) with different time intervals (Fig. 9). In the absence of light or photocatalyst, ABZ was not generated, indicating that NBZ-to-ABZ conversion reactions occurred through a photocatalytic pathway. Fig. 9(a) shows the results of UV-visible absorption spectroscopy of NBZ reduction with $_{0.3}$Ag/CN as a photocatalyst. In the beginning of the reaction, a strong peak was observed at $\lambda$ = 267 nm, which was assigned as the absorption peak of NBZ. Upon light illumination, the reduction reactions occurred very rapidly and the peak intensity for NBZ was reduced, and a new peak appeared at ~230 nm; this new peak was attributed to ABZ. The NBZ peak intensity decreased drastically within 5 min of light illumination and 50% of NBZ was converted to ABZ after 5 min of reaction. The conversion of NBZ increased with irradiation time and reached the maximum (85%) after 180 min. However, 0.5 wt% Ag loading on CN ($_{0.5}$Ag/CN) led to a slight increase in NBZ reduction. After 20 min of reaction, 85% of NBZ was converted to ABZ and the maximum conversion (95%) was attained after prolonged light irradiation for 180 min (Fig. 9(b)). To determine the optimum level of Ag deposition, we carried out experiments using CN with 1 and 2 wt% Ag loadings (Figs. 9(c) and 9(d),

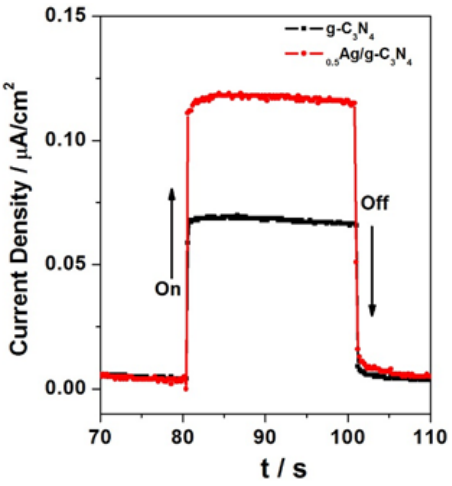


**Fig. 10.** Photocurrent measurement of CN and $_{0.5}$Ag/CN materials under solar simulated light source (one sun condition).

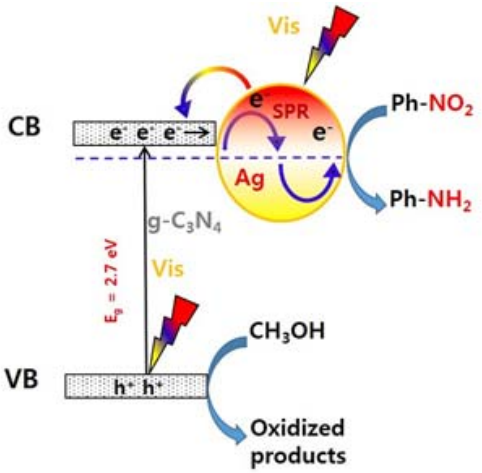


**Fig. 11.** Proposed mechanism for photocatalytic reduction of NBZ to ABZ under visible light irradiation.

respectively). Higher Ag loading led to a decline in the photocatalytic reduction of NBZ to ABZ, likely due to impaired light absorption by excess CN. $_{1}$Ag/CN gave NBZ conversions of 82% and 85% after reaction times of 30 and 60 min, respectively, while $_{2}$Ag/CN gave an NBZ reduction of 71% after a reaction time of 180 min. $_{0.5}$Ag/CN showed the highest conversion efficiency for NBZ reduction, indicating that the optimum level of Ag deposition was 0.5 wt%. Without a co-catalyst or sacrificial agent, no significant activity was observed, indicating the necessity of a Ag co-catalyst and sacrificial agents for the enhancement of photocatalytic NBZ reduction. In addition, photocatalytic reactions of $_{0.5}$Ag/CN were carried out using $C_2H_5OH$ as a sacrificial agent. The conversion efficiency with $_{0.5}$Ag/CN with $CH_3OH$ was higher than those obtained using $C_2H_5OH$. In addition, photocurrent analyses of CN and $_{0.5}$Ag/CN were conducted under simulated solar light (one sun) (Fig. 10). A higher photocurrent response was observed for $_{0.5}$Ag/CN. The addition of Ag nanoclusters to CN enhanced the photocurrent, underscoring the importance of Ag nanoparticles. The higher photocurrent for the Ag-deposited CN photocatalysts indicated that more charge carriers were available in Ag/CN than in CN; the effective utilization of charge carriers would improve the photocatalytic reduction of NBZ to ABZ with $_{0.5}$Ag/CN.

### 3.9. Proposed mechanism

A possible mechanism was suggested on the basis of the experimental data, characterization results obtained from spectroscopy, structural characterization, photoelectrochemical measurements, and literature (Fig. 11). Upon illumination, CN generates electrons and holes. The photoinduced charge carriers are separated through the Ag-CN Schottky barrier (metal-semiconductor interface) of Ag/CN; the introduction of Ag lowers the energy barrier and enhances the conductivity. The Fermi level of Ag is more positive than that of the Conduction Band (CB) of CN because of the shift of the CB level to a more positive value (Bu et al., 2014). In addition, the SPR of Ag metal can induce a local electromagnetic field upon light illumination. The photogenerated electrons in CN

may be trapped by Ag nanoclusters, increasing the separation of charge carriers. The electrons in CN can be transferred to Ag nanoparticles and utilized effectively to reduce the nitro group in NBZ via a six-electron reduction process to generate the target product, ABZ (Dai et al., 2014). The holes in the valence band can react with the hole scavenger, methanol. To determine the source of hydrogen for the reduction of $-NO_2$ to $-NH_2$, we performed a photocatalytic $H_2$ generation reaction in the presence of methanol. Analysis of the gaseous product revealed the generation of $H_2$ molecules, suggesting that they come from water splitting and act as a hydrogen source for $-NO_2$ reduction. Without methanol or any sacrificial agent, there was no significant formation of ABZ, indicating the necessity of a hole scavenger for NBZ reduction. It is noteworthy that, in the absence of a Ag co-catalyst, the degree of NBZ reduction was not significant, suggesting that Ag was an active center for the reduction of NBZ (Roy et al., 2013).

## 4. Conclusions

In the current study, nanoroll-type CN was prepared using a one-pot co-polymerization synthesis protocol without any additional treatment, while an Ag/CN nanocomposite was constructed via the photodeposition (photoreduction) of Ag on CN. The results of several spectroscopy and microscopy techniques confirmed the formation of CN and Ag/CN. Additionally, SEM and HRTEM analyses revealed directly the nanoroll-type morphology of CN and the Schottky junction between Ag and CN in Ag/CN. PL studies indicated fast electron transfer and revealed low-intensity emission features. Highly selective conversion of nitrobenzene to aminobenzene was achieved through a direct reduction process. Ag/CN showed a higher photocurrent performance and ability to reduce toxic NBZ to industrially-valuable ABZ. This study may provide a fundamental route for designing new composites for enhanced photocatalytic performance.

## REFERENCE

An, J., Yang, Q., Luo, Q., Li, X., Yin, R., Liu, F., Wang, D., 2016, Preparation and characterization of silver/g -carbon nitride/chitosan nanocomposite with hotocatalytic activity, Integr. Ferroelectr., 180, 52-60.

Bai, X., Wang, L., Zong, R., Zhu, Y., 2013, Photocatalytic activity enhanced via gC3N4 nanoplates to nanorods, J. Phys. Chem. C, 117, 9952-9961.

Bharad, P. A., Sivaranjani, K., Gopinath, C. S., 2015, A Rational approach towards enhancing solar water splitting: a case study of Au-RGO/N-RGO-$TiO_2$, Nanoscale, 7, 11206-11215.

Bu, Y., Chen, Z., Li, W., 2014, Using electrochemical methods to study the promotion mechanism of the photoelectric conversion performance of Ag-modified mesoporous g-$C_3N_4$ heterojunction material, Appl. Catal. B, 144, 622-630.

Chaiseeda, K., Nishimura, S., Ebitani, K., 2017, Gold nanoparticles supported on alumina as a catalyst for surface plasmon-enhanced selective reductions of nitrobenzene, ACS Omega, 2, 7066-7070.

Chen, Z., Liu, S., Yang, M. Q., Xu, Y. J., 2013, Synthesis of uniform CdS nanospheres/graphene hybrid nanocomposites and their application as visible light photocatalyst for selective reduction of nitro organics in water, ACS Appl. Mater. Inter., 5, 4309-4319.

Dai, X., Xie, M., Meng, S., Fu, X., Chen, X., 2014, Coupled systems for selective oxidation of aromatic alcohols to aldehydes and reduction of nitrobenzene into aminobenzene using CdS/g-$C_3N_4$ photocatalyst under visible light irradiation, Appl. Catal. B, 158-159, 382-390.

Devaraji, P., Gopinath, C. S., 2018, Pt − g-$C_3N_4$ − (Au/$TiO_2$): Electronically integrated nanocomposite for solar hydrogen generation, Int. J. Hydrogen Energ., 43, 601-613.

Devaraji, P., Jo, W. K., 2018, Two-dimensional mixed phase leaf-$Ti_{1-x}Cu_xO_2$ sheets synthesized based on a natural leaf template for increased photocatalytic H2 evolution, Appl. Catal. A, 565, 1-12.

Devaraji, P., Mapa, M., Hakkeem, H. A., Sudhakar, V.,

Krishnamoorthy, K., Gopinath, C. S., 2017, ZnO-ZnS heterojunction: A potential candidate for optoelectronics applications and mineralization of endocrine disruptors in direct sunlight, ACS Omega, 2, 6768-6781.

Devaraji, P., Sathu, N. K., Gopinath, C. S., 2014, Ambient oxidation of benzene to phenol by photocatalysis on $Au/Ti_{0.98}V_{0.02}O_2$: role of holes, ACS Catal., 4, 2844-2853.

European Chemicals Agency, Committee for Risk Assessment, Nitrobenzene ECHA/RAC/CLH-0-0000 002350-87-01/A1, February 3, 2012.

Ge, L., Han, C., Liu, J., Li, Y., 2011, Enhanced visible light photocatalytic activity of novel polymeric g-$C_3N_4$ loaded with Ag nanoparticles, Appl. Catal. A, 409-410, 215-222.

Gholap, S. G., Badiger, M. V., Gopinath, C. S., 2005, Molecular origins of wettability of hydrophobic poly (vinylidene fluoride) microporous membranes on poly (vinyl alcohol) adsorption: surface and interface analysis by XPS, J Phys. Chem. C, 109, 13941-13947.

Grirrane, A., Corma, A., Garcia, H., 2008, Gold catalyzed synthesis of aromatic azo compounds from aminobenzenes and nitroaromatics, Science, 322, 1661-1664.

Guo, S., Deng, Z., Li, M., Jiang, B., Tian, C., Pan, Q., Fu, H., 2016, Phosphorous-doped carbon nitride tubes with a layered micro-nanostructure for enhanced visible-light photocatalytic hydrogen evolution, Angew. Chem. Int. Edit., 55, 1830-1834.

Guo, X., Zhang, G., Cui, H., Wei, N., Song, X., Li, J., Tian, J., 2017, Porous $TiB_2$-TiC/$TiO_2$ heterostructures: synthesis and enhanced photocatalytic properties from nanosheets to sweetened rolls, Appl. Catal. B, 217, 12-20.

Han, Q., Wang, B., Gao, J., Cheng, Z., Zhao, Y., Zhang, Z., Qu, L., 2016, Atomically thin mesoporous nanomesh of graphitic $C_3N_4$ for high-efficiency photocatalytic hydrogen evolution, ACS Nano, 10, 2745-2751.

Ho, W., Zhang, Z., Lin, W., Huang, S., Zhang, X., Wang, X., Huang, Y., 2015, Copolymerization with 2,4,6-triaminopyrimidine for the roll-up the layer structure, tunable electronic properties, and photocatalysis of g$C_3N_4$, ACS Appl. Mater. Inter., 7, 5497-5505.

Jin, Z., Zhang, Q., Yuana, S., Ohno, T., 2015, Synthesis high specific surface area nanotube g-$C_3N_4$ with two-step condensation treatment of melamine to enhance photocatalysis properties, RSC Adv., 5, 4026-4029.

Ke, X., Zhang, X., Zhao, J., Sarina, S., Barry, J., Zhu, H., 2013, Selective reductions using visible light photocatalysts of supported gold nanoparticles, Green Chem., 15, 236-244.

Khan, M. E., Han, T. H., Khan, M. M., Karim, M. R., Cho, M. H., 2018, Environmentally sustainable fabrication of Ag@g-$C_3N_4$ nanostructures and their multi -functional efficacy as antibacterial agents and photocatalysts, ACS Appl. Nano Mater., 1, 2912-2922.

Kimura, K., Naya, S. I., Jin-nouchi, Y., Tada, H., 2012, $TiO_2$ crystal form-dependence of the Au/$TiO_2$ plasmon photocatalyst's activity, J. Phys. Chem. C, 116, 7111-7117.

Kumar, S., Surendar, T., Baruah, A., Shanker, V., 2013, Synthesis of a novel and stable g-$C_3N_4$–$Ag_3PO_4$ hybrid nanocomposite photocatalyst and study of the photocatalytic activity under visible light irradiation, J. Mater. Chem. A, 1, 5333-5340.

Li, H., Gao, Y., Wu, X., Lee, P. H., Shih, K., 2017, Fabrication of heterostructured g-$C_3N_4$/Ag-$TiO_2$ hybrid photocatalyst with enhanced performance in photocatalytic conversion of $CO_2$ under simulated sunlight irradiation, Appl, Surf. Sci., 402, 198-207.

Patra, K. K., Bhuskute, B. D., Gopinath, C. S., 2017, Possibly scalable solar hydrogen generation with quasi-artificial leaf approach, Sci. Rep., 7, 1-9.

Patra, K. K., Gopinath, C. S., 2017, Harnessing visible-light and limited near-IR photons through plasmon effect of gold nanorod with $AgTiO_2$, J. Phys. Chem. C, 122, 1206-1214.

Roy, P., Periasamy, A. P., Liang, C. T., Chang, H. T., 2013, Synthesis of graphene-ZnO-Au nanocomposites for efficient photocatalytic reduction of nitrobenzene, Environ. Sci. Technol., 47, 6688-6695.

Sathu, N. K., Devaraji, P., Gopinath, C. S., 2016, Green leaf to inorganic leaf: a case study of ZnO, J. Nanosci. Nanotechnol., 16, 9203-9208.

Shiraishi, Y., Kanazawa, S., Sugano, Y., Tsukamoto, D., Sakamoto, H., Ichikawa, S., Hirai, T., 2014, Highly

selective production of hydrogen peroxide on graphitic carbon nitride ($gC_3N_4$) photocatalyst activated by visible light, ACS Catal., 4, 774-780.

Tada, H., Ishida, T., Takao, A., Ito, S., Mukhopadhyay, S., Akita, T., Tanaka, K., Kobayashi, H., 2005, Kinetic and DFT studies on the $Ag/TiO_2$-photocatalyzed selective reduction of nitrobenzene to aminobenzene, Chemphyschem, 6, 1537-1543.

Tahir, M., Cao, C., Mahmood, N., Butt, F. K., Mahmood, A., Idrees, F., Hussain, S., Tanveer, M., Ali, Z., Aslam, I. 2014, Multifunctional $gC_3N_4$ nanofibers: a template -free fabrication and enhanced optical, electrochemical, and photocatalyst properties, ACS Appl. Mater. Inter., 6, 1258-1265.

Tanaka, A., Nishino, Y., Sakaguchi, S., Yoshikawa, T., Imamura, K., Hashimoto, K., Kominami, H., 2013, Functionalization of a plasmonic $Au/TiO_2$ photocatalyst with an Ag co-catalyst for quantitative reduction of nitrobenzene to aminobenzene in 2-propanol suspensions under irradiation of visible light, Chem. Commun., 49, 2551-2553.

Toyao, T., Saito, M., Horiuchi, Y., Mochizuki, K., Iwata, M., Higashimura, H., Matsuoka, M., 2013, Efficient hydrogen production and photocatalytic reduction of nitrobenzene over a visible-light-responsive metal–organic framework photocatalyst, Catal. Sci. Technol., 3, 2092-2097.

Verma, S., Baig, R. B. N., Nadagouda, M. N., Varma, R. S., 2017, Hydroxylation of benzene via-C-H activation using bimetallic $CuAg@g\text{-}C_3N_4$, ACS Sustainable Chem. Eng., 5 3637-3640.

Xiao, Q., Sarina, S., Waclawik, E. R., Jia, J., Chang, J., Riches, J. D., Wu, H., Zheng, Z., Zhu, H., 2016, Alloying gold with copper makes for a highly selective visible-light photocatalyst for the reduction of nitroaromatics to aminobenzenes, ACS Catal., 6, 1744-1753.

Yang, Z., Xu, X., Liang, X., Lei, C., Cui, Y., Wu, W., Yang, Y., Zhang, Z., Lei, Z., 2017, Construction of heterostructured $MIL\text{-}125/Ag/g\text{-}C_3N_4$ nanocomposite as an efficient bifunctional visible light photocatalyst for the organic oxidation and reduction reactions, Appl. Catal. B, 205, 42-54.

Zhang, Y., Liu, J., Wu, G., Chen, W., 2012, Porous graphitic carbon nitride synthesized via direct polymerization of urea for efficient sunlight-driven photocatalytic hydrogen production, Nanoscale, 4, 5300-5303.

Zhu, H., Ke, X., Yang, X., Sarina, S., Liu, H., 2010, Reduction of nitroaromatic compounds on supported gold nanoparticles by visible and ultraviolet light, Angew. Chem. Int. Ed., 49, 9657–9661.

• Post-Doctoral Fellow. Perumal Devaraji
Department of Environmental Engineering, Kyungpook National University
devjichemist@gmail.com
• Professor. Wan-Kuen Jo
Department of Environmental Engineering, Kyungpook National University
wkjo@knu.ac.kr